

Coupled THM modelling of engineered barriers for the final disposal of spent nuclear fuel isolation

ERDEM TOPRAK^{1*}, SEBASTIA OLIVELLA² & XAVIER PINTADO³

¹*International Centre for Numerical Methods in Engineering (CIMNE), Universidad Politècnica de Catalunya, Campus Norte UPC, 08034 Barcelona, Spain*

²*Department of Geotechnical Engineering and Geosciences, Universidad Politècnica de Catalunya, Campus Norte UPC, 08034 Barcelona, Spain*

³*B + TECH Oy, Laulukuja 4, 00420 Helsinki, Finland*

*Correspondence: erdem.toprak@upc.edu

Abstract: This paper describes the thermohydromechanical (THM) simulation of engineered barrier systems (EBS) for the final disposal of nuclear spent fuel in Finland. The bentonite barriers were simulated with the Barcelona Basic Model and the model was calibrated from laboratory tests. The evolution of gap closure and the presence of a fracture intersecting the disposal were analysed. The simulations were performed in 2D axisymmetrical geometries. Full 3D simulations were carried out in order to check the effect of the third dimension. The time required for the barriers to reach full saturation, the maximum temperature, deformations and displacements at the buffer–backfill interface and the homogenization of components both locally and globally are the main interests. The effect of rock fracture and the hydraulic conductivity of the rock are subjected to 2D sensitivity analyses.



Gold Open Access: This article is published under the terms of the CC-BY 3.0 license

The final disposal of nuclear spent fuel in crystalline bedrock is developing in Finland. Olkiluoto bedrock was proposed as the site for the repository (Posiva 2013). The disposal is based on the use of multiple release barriers, which ensures that the nuclear spent fuel cannot be released into the biosphere or become accessible to humans. The release barriers include the physical state of the fuel, the disposal canister, the bentonite buffer, the backfilling of the tunnels and the surrounding rock.

The KBS-3V concept (Posiva 2013) consists of deposition holes spaced between 7.5 and 11 m of each other in backfilling tunnels excavated at a depth of approximately 400–450 m and located at approximately 25 m from each other (Fig. 1). The spent nuclear fuel will be encapsulated in final disposal canisters made of cast iron and enclosed in a copper shell. These canisters will be placed in the deposition holes and surrounded with bentonite clay, which protects the canister from any potential jolt in the bedrock and slows down the movement of water in the proximity of the canister.

Mechanical constitutive model for clay-based materials

In this section, constitutive model calibration is described. The calibration was performed by

modelling the results from oedometer tests and infiltration tests in buffer and backfill materials: MX-80 bentonite (buffer blocks: Kiviranta & Kumpulainen 2011; Juvankoski *et al.* 2012; Pintado & Rautioaho 2013), Friedland clay (backfill blocks: Keto *et al.* 2013; Kiviranta *et al.* 2016) and pellets (Juvankoski *et al.* 2012).

In this paper, buffer (MX-80 bentonite), backfill (Friedland clay) and pellets are modelled using the Barcelona Basic Model (BBM) originally described in Alonso *et al.* (1990). This model is briefly described here. Elastic, isotropic, non-isothermal volumetric strains are defined by:

$$d\varepsilon_v^e = \frac{\kappa_i}{1+e} \frac{dp'}{p'} + \frac{\kappa_s}{1+e} \frac{ds}{s+0.1} + \alpha dT, \quad (1)$$

where e is the void ratio, κ_i , κ_s and α are parameters, p' is net mean stress, s is suction and T is temperature. For deviatoric elastic strains, a constant Poisson ratio is used.

Plasticity is accounted for using a Modified Cam-Clay yield surface (and plastic potential) with the following equation:

$$F = q^2 - M^2(p' + p_s)(p_0 - p') = 0, \quad (2)$$

where $p_s = ks$ and p_0 correspond to the intersection of the ellipse with the p' -axis, q is the equivalent

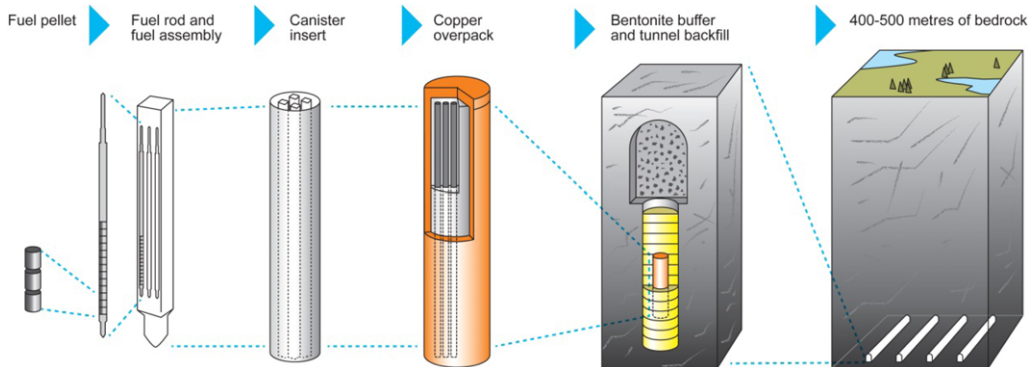


Fig. 1. A possible design of the final disposal facility (KBS-3) planned to be constructed at the Olkiluoto site.

shear stress, and M and k are parameters. The pre-consolidation mean net stress (p_o) is a function of suction in the BBM with the following form:

$$p_o(s) = p^c \left(\frac{p_o^*}{p^c} \right)^{\frac{\lambda(0) - \kappa}{\lambda(s) - \kappa}}, \quad (3)$$

where p^c is the reference stress of the loading-collapse curve, p_o^* is the initial yield mean net stress, $\lambda(0)$ is the slope of the virgin elastoplastic compressibility for saturated conditions of the soil and κ is the slope of the unload-reload line (elastic response). The function $\lambda(s)$ is the slope of the virgin elastoplastic compressibility for a given suction (volumetric compressibility index), written as:

$$\lambda(s) = \lambda(0)[(1 - r) \exp(-\beta s) + r], \quad (4)$$

where r and β are parameters.

Finally, the hardening law for the BBM is given as:

$$dp_o^* = \frac{1 + e}{\lambda(0) - \kappa} p_o^* d\varepsilon_v^p, \quad (5)$$

where $d\varepsilon_v^p$ is the plastic volumetric strain increment.

Hydraulic and thermal constitutive models

The fluid flow is governed by Darcy's law, given as:

$$\mathbf{q}_l = -\frac{\mathbf{k}k_{rl}}{\mu_l} (\nabla P_l - \rho_l \mathbf{g}), \quad (6)$$

where \mathbf{q}_l is the volumetric flux of liquid, \mathbf{k} is the intrinsic permeability tensor, k_{rl} is the phase relative permeability, μ_l is the viscosity of the fluid, P_l is the pressure of the fluid and ρ_l is the density of

the fluid. Relative permeability is calculated as a power of the degree of saturation:

$$k_{rl} = S_l^m, \quad (7)$$

where S_l is the degree of saturation and m is a parameter. The degree of saturation for the liquid phase is calculated using the retention curve with the relationship of Van Genuchten (1980); this is written as:

$$S_e = \frac{S_l - S_{rl}}{S_{ls} - S_{rl}} = \left[1 + \left(\frac{P_g - P_l}{P} \right)^{1/(1-\lambda)} \right]^{-\lambda}, \quad (8)$$

where S_e is the effective degree of saturation of porous media, S_l is the degree of saturation of liquid, S_{rl} is the residual degree of saturation, S_{ls} is the maximum degree of saturation, P_g is the gas pressure, P_l is the liquid pressure, λ is the shape function coefficient for the retention curve and P is a parameter that can be interpreted as the pressure of air entrance.

The molecular diffusion of vapour is governed by Fick's law:

$$\mathbf{i}_g^w = -\left(\tau \phi \rho_g S_g D_g^w \mathbf{I} \right) \nabla \omega_g^w, \quad (9)$$

where \mathbf{i}_g^w is the non-advective mass flux vector, ϕ is the porosity of porous media, ρ_g is the density of the gas phase, S_g is the degree of saturation of the gas phase, D_g^w is the molecular diffusion coefficient for vapour in the gas phase, ω_g^w is the mass fraction of vapour in the gas phase, \mathbf{I} is the identity tensor and τ is a tortuosity coefficient.

The diffusion coefficient of vapour is given by:

$$D_g^w = D^v \frac{(273.15 + T)^n}{P_g}, \quad (10)$$

where D^v is the coefficient of diffusion ($5.9 \times 10^{-6} \text{ m}^2 \text{ s}^{-1} \text{ K}^{-n} \text{ Pa}$) and n is a parameter ($n = 2.3$).

COUPLED THM MODELLING

For the air gap element, it is convenient that retention properties evolve as the gap closes. In order to represent this response using the available functions in CODE_BRIGHT, the dependence of the retention curve on porosity has been taken into account when considering the following equation:

$$P(\phi) = P \exp(a(\phi_0 - \phi)), \quad (11)$$

where a is a parameter. This function allows a low retention capacity for the gap to be used when it is open (very small saturation), which evolves into a higher retention capacity for the gap as it closes (closer or similar to what occurs in the surrounding clay).

The heat transfer process is governed by Fourier's law, given as the heat flux vector:

$$\mathbf{i}_c = -\lambda \nabla T, \quad (12)$$

where thermal conductivity depends on the degree of saturation in the following way:

$$\lambda = \lambda_{\text{sat}} S_1 + \lambda_{\text{dry}} (1 - S_1), \quad (13)$$

where \mathbf{i}_c is the conductive flux vector of heat, T is the temperature, λ is the thermal conductivity, λ_{sat} is the thermal conductivity of the water-saturated porous medium, λ_{dry} is the thermal conductivity of the dry porous medium and S_1 is the degree of saturation.

For the thermal analysis, the required parameters for the materials are the thermal conductivity (λ), the specific heat (c_s) and the solid density (ρ_s).

Material properties

Friedland clay was chosen as the reference material for manufacturing the backfill blocks (Keto *et al.* 2013). Although the backfill consists of different components (i.e. a foundation bed, blocks and pellets) (Fig. 2), it is treated as a single material.

It was planned that the pellets be installed between the buffer blocks and rock (Juvankoski *et al.* 2012), and that the pellets would occupy a volume of 10–20% of the excavation volume associated with the deposition holes. It is also anticipated that the pre-compacted buffer blocks would swell and compress the pellet component. As a result of this, it was anticipated that the buffer block–pellet material in the tunnel should meet the performance requirements of the buffer described in Juvankoski *et al.* (2012).

In many aspects, it can be said that the pellet component is, in fact, a simple filler of the space between the buffer and the rock. There are several reasons for using fillers in gap. Fillers can secure better thermal conductivity and prevent spalling of

the surrounding rock into the deposition hole. Also fillers might be needed in order to retain an adequate average density (Marjavaara & Kivikoski 2011).

In order to determine the hydromechanical parameters of the buffer (MX-80) and backfill (Friedland clay), an experimental programme was followed. Table 1 summarizes the initial properties of the materials for each test considered. For each material, an oedometer and an infiltration test was performed.

Figure 3 shows the calibration results from the oedometer test data for Friedland clay (backfill) (Fig. 3a) and MX-80 bentonite (buffer) (Fig. 3b). As the samples were initially unsaturated, there was a stabilization (flooding) process at the beginning of the oedometer tests. It can be seen that both materials showed considerable expansive behaviour before loading. Once the saturation took place, samples were exposed to loading and unloading phases. In this study, the Barcelona Basic Model (Alonso *et al.* 1990) parameters used in Toprak *et al.* (2013) for MX-80 bentonite clay have been updated. The BBM parameters for MX-80 bentonite and Friedland clay were obtained by calibration of the oedometer tests. For the pellets, a preliminary set of parameters that take into account non-linear elasticity was established. The pellets represent a small volume fraction of the total volume of the clay barrier. The calibrated BBM parameters that were used in the 2D and 3D modelling of MX-80 bentonite, Friedland clay and the pellets are given in Table 2.

Figure 4 shows the final distribution of the water content and the infiltration tests set up for Friedland clay (Fig. 4a) and MX-80 bentonite (Fig. 4b) at the end of the experiment. The infiltration cell was made of stainless steel. The inner diameter of the infiltration cell was 50 mm and the height of the sample was approximately 63 mm. There were two sintered porous frits made of stainless-steel balls, with a diameter of 10 μm , at the top and bottom of the sample. The materials (MX-80 bentonite and Friedland clay) were placed directly inside the cells. During the tests, a target water pressure was imposed at the bottom of the sample using a pressure–volume controller manufactured by GDS (<http://www.gdsinstruments.com>). On the other side, the water pressure was zero (the atmospheric pressure was fixed as the origin). The tests were performed at laboratory temperature (approximately 24°C). The suction of the materials was measured before the tests using a chilled mirror psychrometer WP-4 (<http://www.decagon.com>). The sample volume was kept constant during the test. The water inlet flow was measured continuously. At the end of the test, the sample was cut into slices with a saw. After cutting the sample, the water content was measured.

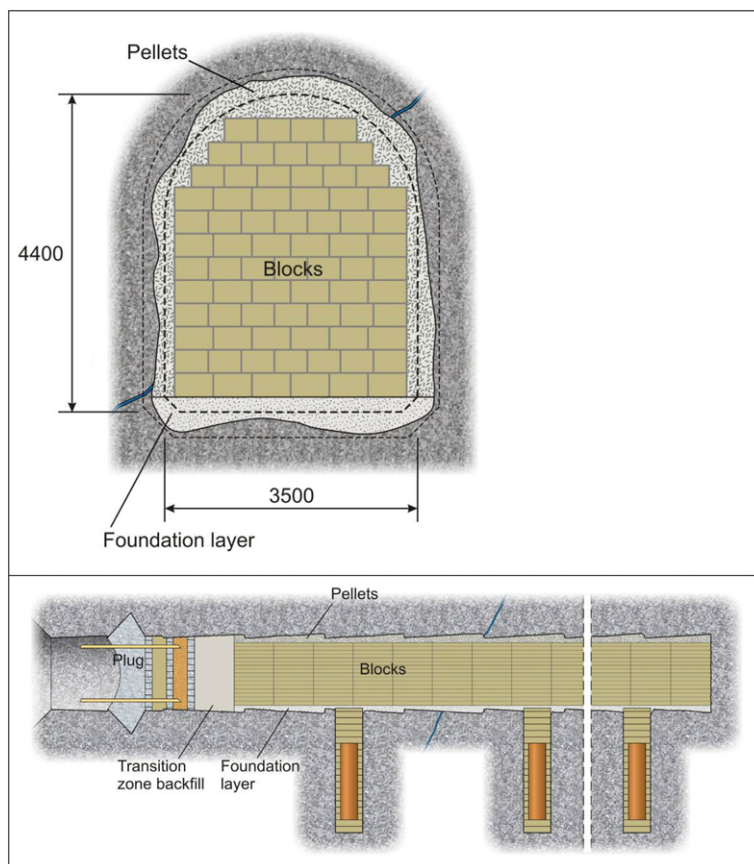


Fig. 2. Schematic figures showing the main backfill components (foundation layer, backfill blocks and pellets).

The swelling near the injection zone is possible because other parts of the sample undergo compression. Some level of suction is still measured at the end of the test. This could be due to the fact that the sample was not fully saturated, and dismantling of the sample with an associated unloading induces some suction. The hydraulic parameters of MX-80 bentonite and Friedland clay were calibrated from these infiltration tests and are listed in Table 3.

The host rock (Hagos *et al.* 2003) and the canister (Raiko 2012) are considered to be linear elastic with parameters E , ν and α , respectively, for Young's (elastic) modulus, Poisson's ratio and the coefficient of thermal expansion. Hydraulic and mechanical properties of the host rock and canister are given in Tables 3 and 4, together with the properties of the gap.

Mechanical parameters for the air gap were proposed in Toprak *et al.* (2013). The 10 mm air gap

Table 1. Initial conditions for materials in the infiltration and oedometer tests

Material	Test	Initial dry density (kg m^{-3})	Initial water content (%)	Initial degree of saturation (%)	Test duration (days)
MX-80 bentonite	Oedometer	1600	6.04	25	191
Friedland clay	Oedometer	1950	8.9	59	243
MX-80 bentonite	Infiltration	1700	5.33	23.34	68
Friedland clay	Infiltration	1750	7.7	37	13

COUPLED THM MODELLING

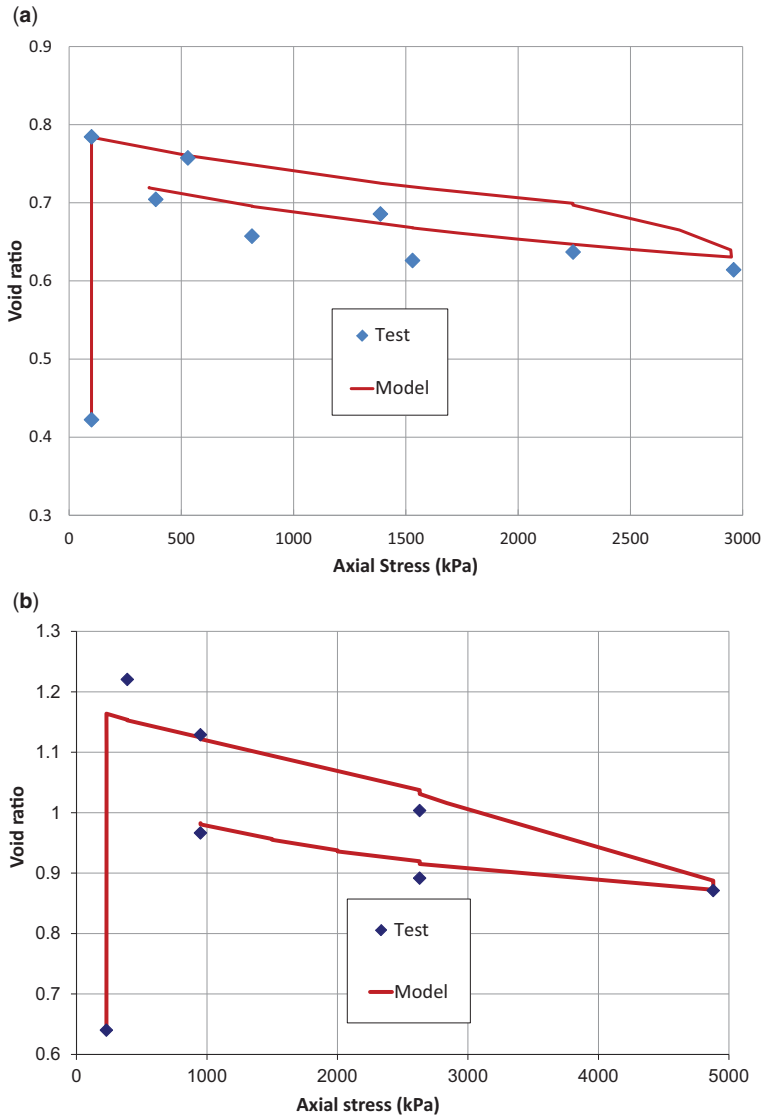


Fig. 3. Void ratio *v.* effective axial stress in (a) Friedland clay and (b) MX-80 bentonite. During an oedometer test, inundation of the sample produces a large initial swelling.

(between the canister and buffer) was modelled for simplicity using a bi-linear elasticity model that uses two values of Young's modulus: one for the opened gap and the other for the closed gap. A large value of Young's modulus (E_c) was used for the closed gap (representing the contact between gap surfaces) and a relatively low value (E_o) was used for the open gap. Compression strain was used to check whether the gap was open or closed. As, during the calculations, the gap undergoes a path from an initially open state towards a closed

state as the buffer swells, the approximation considered was deemed to be adequate.

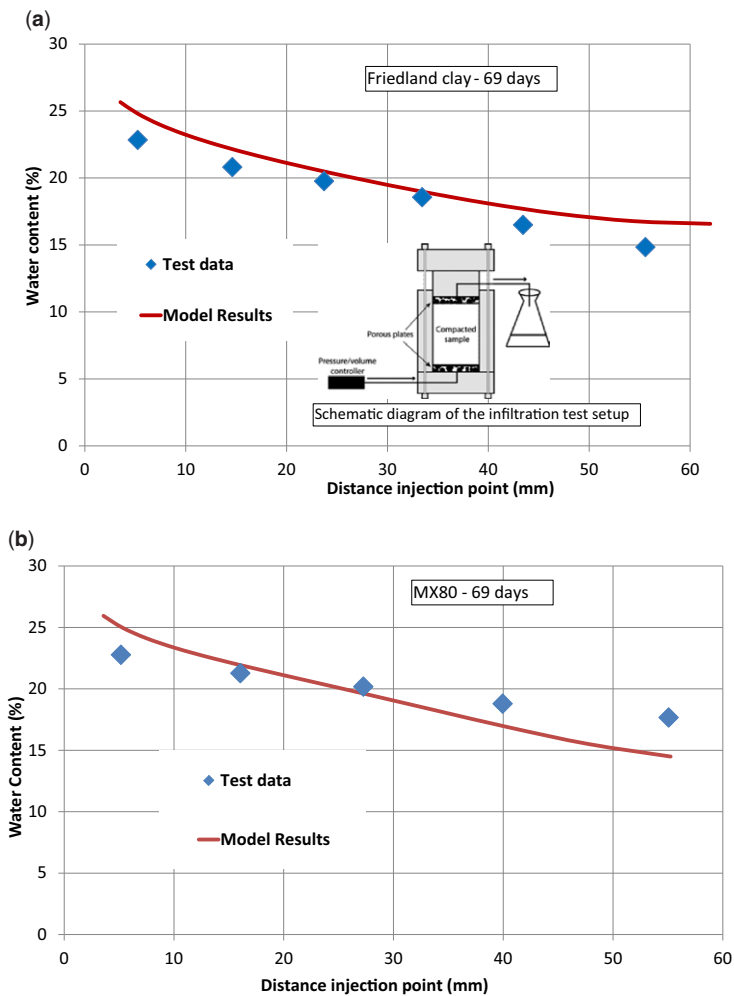
Finally, typical thermal properties for all the materials are given in Table 5.

Governing equations

The equation of equilibrium of forces (or stresses), the equation of mass balance of water and the equations of mass balance of energy were solved

Table 2. *BBM parameters for MX-80 bentonite, Friedland clay and pellets*

Parameter	Symbol	MX-80 bentonite	Friedland clay	Pellets
Poisson ratio (–)	ν	0.3	0.3	0.3
Minimum bulk module (MPa)	K_{\min}	10	10	10
Parameters for elastic volumetric compressibility against mean net stress change (–)	κ_{i0}	0.09	0.05	0.03
Parameters for elastic volumetric compressibility against suction change (–)	κ_{s0}	0.09	0.05	0.03
Slope of void ratio – mean net stress curve at zero suction (–)	$\lambda(0)$	0.25	0.18	–
Parameters for the slope void ratio – mean net stress at variable suction (–, MPa^{-1})	r	0.8	0.8	–
	β	0.02	0.02	–
Reference pressure for the P_0 function (MPa)	p^c	0.1	0.1	–
Pre-consolidation mean stress for saturated soil (MPa)	P_o^*	2	2	–
Critical state line (–)	M	1.07	1.07	–

**Fig. 4.** Water content v. distance to the injection point for infiltration tests on (a) Friedland clay and (b) MX-80 bentonite.

COUPLED THM MODELLING

Table 3. Hydraulic parameters for materials

Equation	Parameter	Rock	Friedland clay	MX-80 bentonite	Pellets	Gap element
Van Genuchten retention curve	P (MPa)	1.5	25	31.25	31.25	0.001
	λ (-)	0.3	0.4	0.5	0.5	0.5
Advective flux (Darcy)	a (-)					10
	k (m ²)	1.5×10^{-19} or 3.5×10^{-20}	1.6×10^{-20}	5.6×10^{-21}	5.6×10^{-20}	10^{-16}
Diffusive flux (Fick)	m (-)	3	3	3	3	3
	τ (-)	0.4	0.4	0.4	0.4	0.4

simultaneously to obtain displacements, pressure and temperature at each point and time of the model. The formulation can be found elsewhere: for instance, in Olivella *et al.* (1994, 1996).

Modelling of vertical disposal schemes

The model geometry and materials are shown in Figure 5a. This figure shows boundary conditions that are both hydraulic (Fig. 5b) and mechanical (Fig. 5c). The analysis assumed under axisymmetrical conditions.

The initial water pressure for all materials in the deposition hole was -41 MPa. The initial temperature was 10.5°C throughout the domain modelled. The rock had a hydrostatic water pressure (with $P_1 = 4.36$ MPa at $z = 436$ m and $P_1 = 3.98$ MPa at $z = 398$ m, where z is the depth below the surface), which was maintained along with corresponding boundary conditions. The temperature at the boundaries is seen to evolve with time (Fig. 6a). This temperature can be calculated from an analytical solution that takes into account the presence of all canisters (Ikonen 2003). An initial confining stress of 10.6 MPa was considered for the host rock. This confining pressure was also used as a boundary condition (applied on the top boundary). The lateral and bottom boundaries had prescribed normal displacements. During the excavation process (assumed to be 1 year), a prescribed liquid pressure (-5 MPa) was applied to the excavation surface to represent the process of

ventilation. This boundary condition was removed when the buffer and backfill materials were emplaced. During the simulated time period, the hydrostatic liquid pressure was imposed on the top and bottom boundaries.

Regarding the power evolution of the canister, there are two main parameters playing a fundamental role, these are the residual power at the time of deposition and the decay rate. The work by Hökmark *et al.* (2009) was taken as a reference for the calculation of the power and the decay heat rate. The power as a function of time for an individual canister can be expressed as:

$$P(t) = P(0) \sum_{i=1}^7 a_i \exp(-t/t_i). \quad (14)$$

In this expression, $P(0)$ is the canister power at the time of deposition, and a_i and t_i are parameters. Two parameter sets from SKB of power data relative to the time of cooling prior to disposal are given in Table 6. A burnup of 38 MWd/kg U (megawatt days per kg of uranium) is used as a reference.

The coefficients given in Table 6 are valid for an initial power level of 1837.3 W (in the case of 30 year-old fuel) and an initial power level of 1545.3 W (in the case of 40 year-old fuel). The work presently being performed is targeting a 1700 W initial power level at the time of deposition. The power function and the prescribed temperatures used in the models presented here are shown in Figure 6.

Table 4. Mechanical parameters for air-gap element, rock and canister

Parameter	Rock	Canister	Parameters	Gap element
E (MPa)	65 000	21 000	E_c (MPa)	1000
ν	0.25	0.3	ν	0.3
α ($^\circ\text{C}^{-1}$), linear	10^{-5}	10^{-5}	α ($^\circ\text{C}^{-1}$), linear	-
			E_o (MPa)	1
			Strain limit	0.95

Table 5. Thermal parameters for materials

Parameter	Rock	Canister	Backfill	Bentonite	Pellets	Gap element
ρ_s (kg m ⁻³)	2749	7800	2780	2780	2780	–
ϕ_o	0.02	0.01	0.4604	0.438	0.669	0.8
c_s (J kg ⁻¹ K ⁻¹)	784	450	800	800	800	–
λ_{dry} (W m ⁻¹ K ⁻¹)	2.61	390	0.3	0.3	0.3	0.045
λ_{sat} (W m ⁻¹ K ⁻¹)	2.61	390	1.3	1.3	1.3	0.6

Values of 1700 W of canister power, 25 m of tunnel spacing and 11 m of canister spacing, and variable temperatures at the boundaries (Fig. 6a, b) were used to perform the thermohydraulic (THM) calculations (see Toprak *et al.* 2013 for detailed information on thermal calculations under axisymmetrical conditions).

With the formulation and parameters decided, a series of THM calculations were carried out using a 2D axisymmetrical configuration, as well as using a 3D configuration. For the 2D axisymmetrical configuration, three cases described in Keto *et al.* (2013) were been considered. Each one has been given a name depending on the hydraulic

properties chosen for the host rock, and one case includes a higher permeability zone representing a fracture. The cases are:

- Normal deposition hole (Normal_Case). The rock hydraulic conductivity is 1.52×10^{-12} m s⁻¹ (equivalent to 1.52×10^{-19} m² of intrinsic permeability). Assuming water density of $\rho = 1000$ kg m⁻³, water viscosity $\mu = 0.001$ Pa s and gravity $g = 10$ N kg⁻¹, gives the following conversion: $K = (\rho g / \mu) k = 1000 \times 10 / 0.001 k$: that is, K (m s⁻¹) = $10^7 k$ (m²), where K is hydraulic conductivity and k is intrinsic permeability. The rock is considered

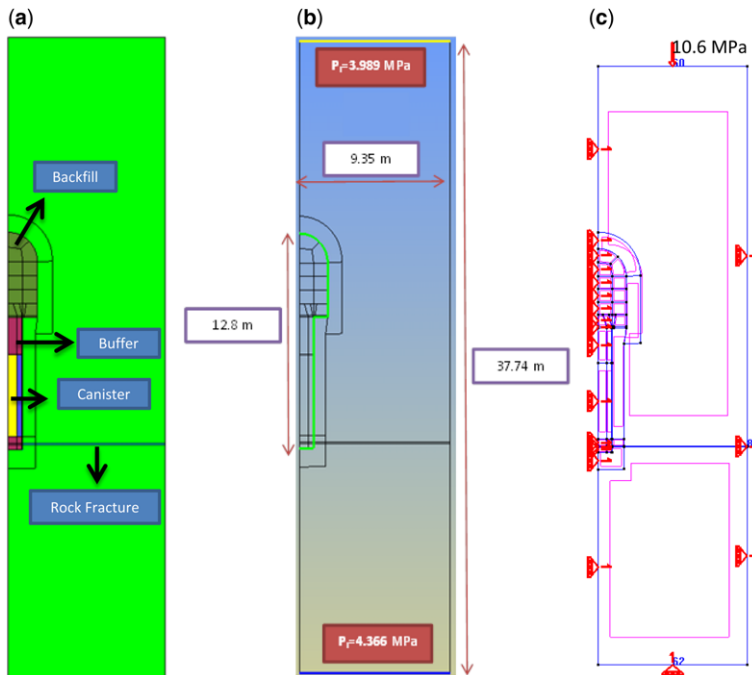


Fig. 5. (a) Geometry and materials, and (b) and (c) boundary conditions for the 2D models. Fracture is considered only in the wet case. The buffer consists of buffer blocks, buffer ring and pellets. Water pressure is prescribed only on the top and bottom of the model in (b), while vertical surfaces are assumed impermeable due to symmetry. Normal displacements are prescribed on the bottom and lateral surfaces, while a constant stress is applied on the top in (c).

COUPLED THM MODELLING

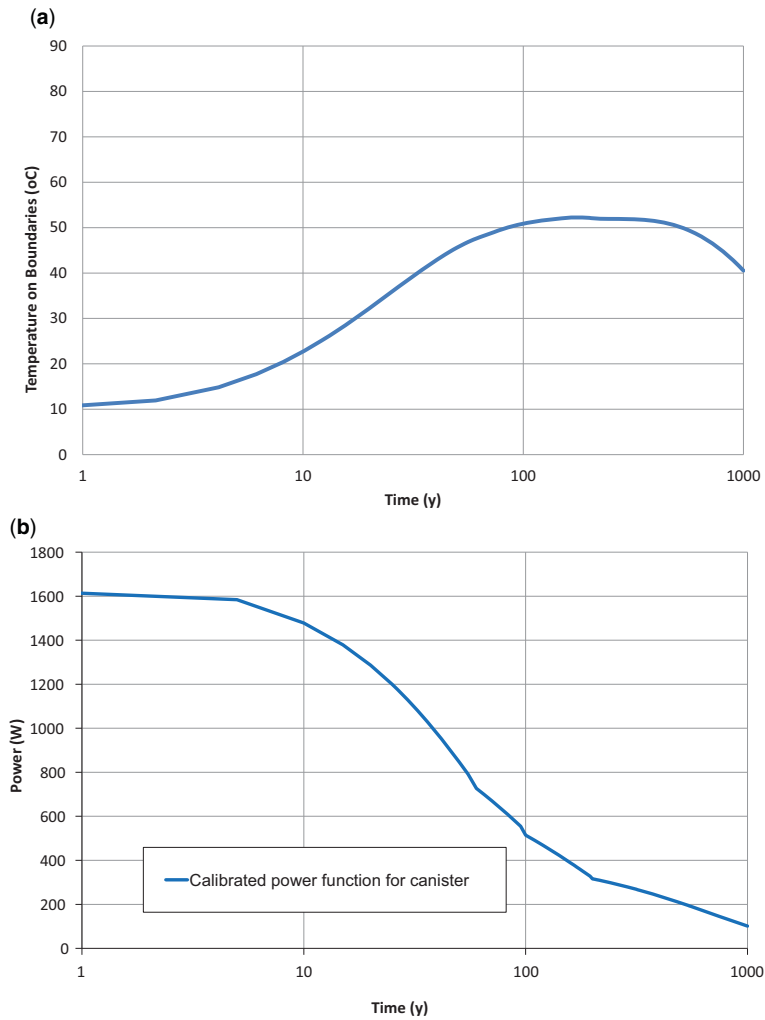


Fig. 6. (a) Temperature calculated from an analytical model (Ikonen 2003) prescribed on the top and bottom boundaries, and (b) power of the canister considered.

Table 6. Parameters for the exponential equation for canister power calculations

I	t_i (years)	a_i (30 years)	a_i (40 years)
1	20	0.070	0.049
2	50	0.713	0.696
3	200	-0.051	-0.059
4	500	0.231	0.271
5	2000	0.024	0.027
6	5000	-0.009	-0.010
7	20 000	0.022	0.026

For 30 year-old fuel, $P(0) = 1837.3$ W. For 40 year-old fuel, $P(0) = 1545.3$ W.

homogeneous: that is, no fracture is considered. This value of intrinsic permeability is considered to be a standard value for the rock at the repository conditions.

- Wet deposition hole (Wet_Case). In this case, the rock hydraulic conductivity is $1.52 \times 10^{-12} \text{ m s}^{-1}$ (equivalent to $1.52 \times 10^{-19} \text{ m}^2$ of intrinsic permeability) and a predefined fracture was considered with a transmissivity of $1.1 \times 10^{-9} \text{ m}^2 \text{ s}^{-1}$. The fracture (high conductive zone) is horizontal because for the axisymmetrical geometry, it is not possible to represent inclined surfaces. The fracture thickness considered is 8 cm in order to avoid elements that are too

small. The fracture is modelled with continuum elements. The equivalent hydraulic conductivity of the fracture is $1.37 \times 10^{-8} \text{ m s}^{-1}$ ($1.37 \times 10^{-15} \text{ m}^2$ of intrinsic permeability).

- Dry deposition hole (Dry_Case). The rock hydraulic conductivity is $3.53 \times 10^{-13} \text{ m s}^{-1}$ (equivalent to $3.53 \times 10^{-20} \text{ m}^2$ of intrinsic permeability). In order to get drier conditions, the intrinsic permeability of the rock is reduced by approximately one order of magnitude, compared to the so-called normal case.

Figure 7 shows the hydraulic boundary conditions and intrinsic permeability for the three cases. In the case of the wet deposition tunnel, there is a zone with higher conductivity representing a fracture, and an appropriate boundary condition is applied at the end of the fracture. The temperature of water inflow through the fracture is the temperature in the lateral boundary (no heat-flow boundary condition). As indicated in Figure 7, the rock is less

permeable in the dry deposition case compared to the wet and normal cases.

There are three critical zones that are considered relevant in this THM model, these are: (1) 'the buffer-backfill interface' (Åkesson *et al.* 2010; Leoni 2013), where the vertical displacements show the largest values; (2) 'canister wall in contact with the buffer', the maximum temperature of the engineered barrier is reached on this surface (Ikonen 2003), and desaturation of the buffer takes place because of intense heating from the canister; and (3) 'buffer blocks under the canister', the maximum stresses are achieved here owing to the combination of the canister weight and swelling of the clay materials.

Results for 2D axisymmetrical modelling

Figure 8 shows the temperature evolution in the canister. The temperature increases due to heat

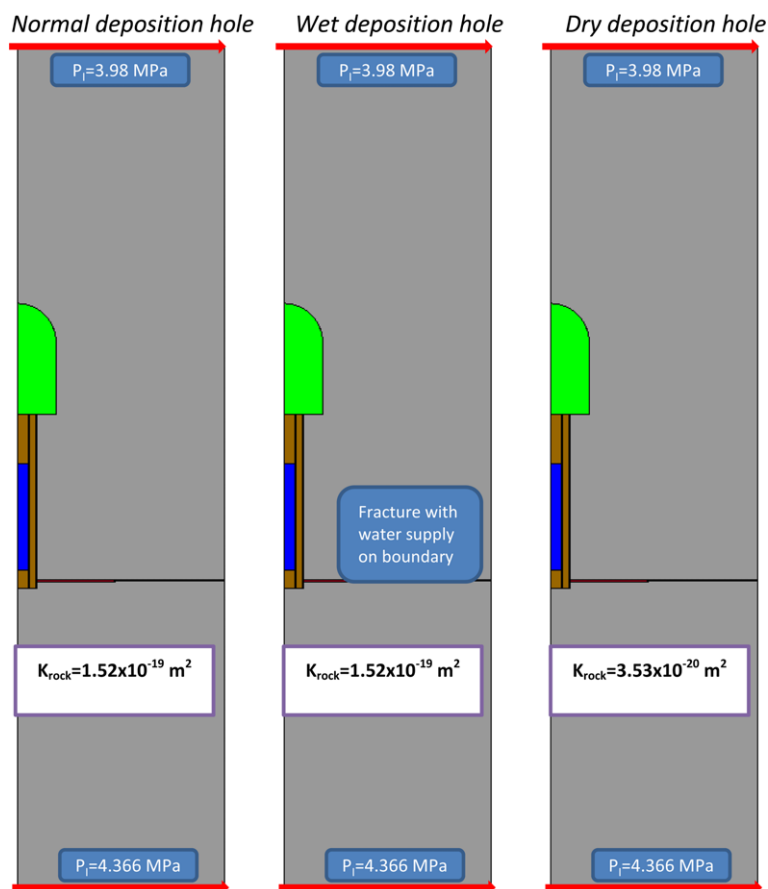


Fig. 7. Properties and boundary conditions for the fracture in three cases.

COUPLED THM MODELLING

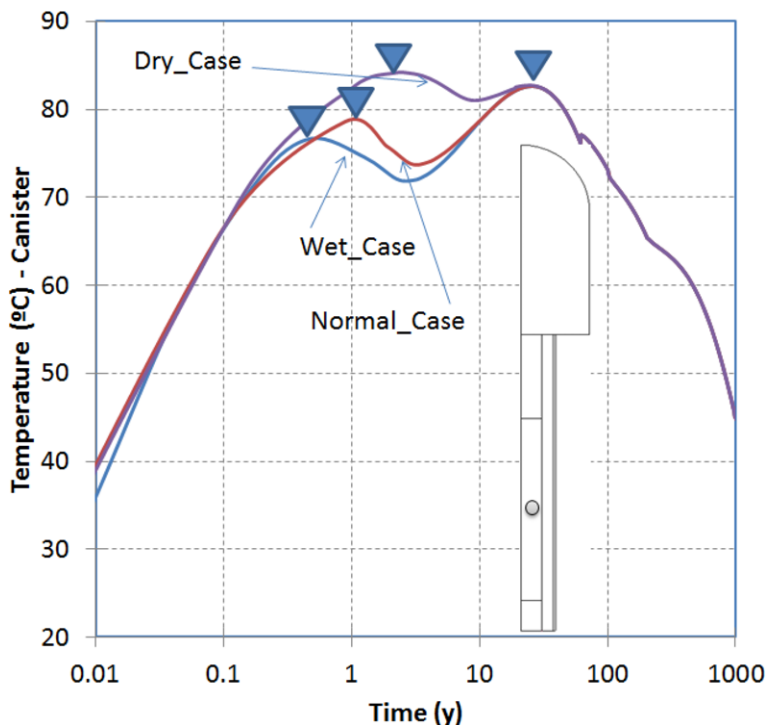


Fig. 8 Evolution of temperature in three cases (location: canister). Time from canister emplacement. The triangles indicate the local and global maxima for each curve.

generation in the canister, which, as shown in Figure 6, is characterized by decay to half-value in about 70–80 years. For the geometry considered, a peak value above 80°C takes place and the temperature decreases afterwards. However, the shape of the temperature evolution in the canister is influenced by the water saturation of the different components of the barrier and the presence of the gap. Both heat capacity and thermal conductivity depend on the degree of saturation.

The maximum temperature is not significantly influenced by the hydration conditions in general, but the evolution at earlier times is different due to the effect of the gap and saturation conditions of the barrier components. The gap under dry conditions produces thermal isolation as it remains open (air has lower heat transport capacity than water or soil). When the rock intrinsic permeability is very low (Dry_Case), the gap closure is delayed and the temperature in the canister increases due to the isolation effect. For the Dry_Case, the maximum temperature in the canister is higher, by a few degrees compared to the other cases and occurs in a different peak that occurs earlier. The peak that occurs around 1 year is caused by the presence of the gap, so the temperature decrease after that

peak is motivated by the increase in conductivity induced by the combined effect of saturation and closure. The peak caused by the gap closure occurs earlier than the peak caused by the decaying power function.

Figure 9 shows the evolution of the liquid pressure for the three cases in the bentonite ring adjacent to the canister. In the case of the wet deposition hole, as the global intrinsic permeability (including the fracture) is higher compared with the other cases, the saturation of materials takes place faster. Desaturation of the bentonite ring is much greater in the Dry_Case because the rock intrinsic permeability is lower than in the other cases, and this implies a lower thermal conductivity of the dried-up buffer (Börgesson *et al.* 1994; Tang *et al.* 2007; Pintado *et al.* 2013).

With regard to stress development, the most critical zone is below the canister where the stresses become greater. Figure 10 shows the swelling pressure of buffer blocks under the canister for the three cases. Stress increases as liquid pressure evolves from extremely negative values caused by heating towards zero and positive values (i.e. hydration produced by a water supply from the host rock). The effect of the fracture is clearly observed in Figure 10,

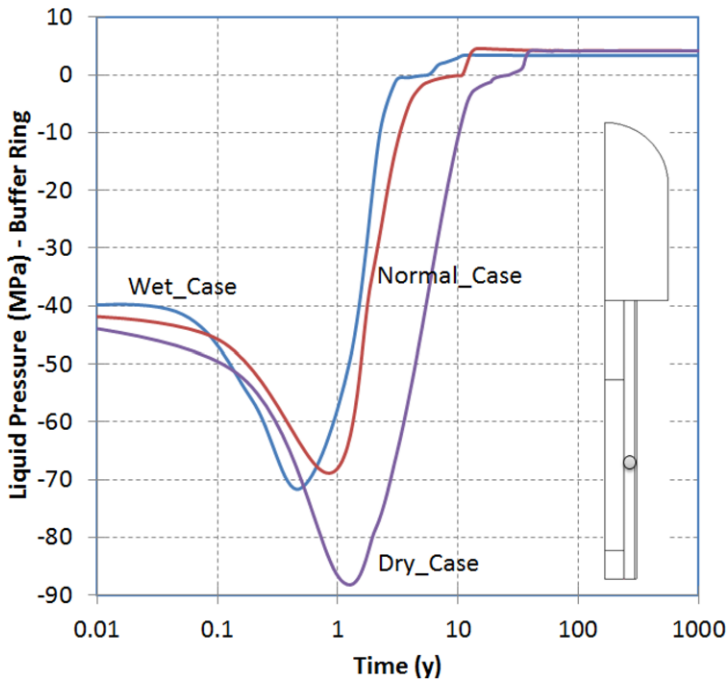


Fig. 9 Evolution of liquid pressure in three cases (location: buffer ring). Time from canister emplacement.

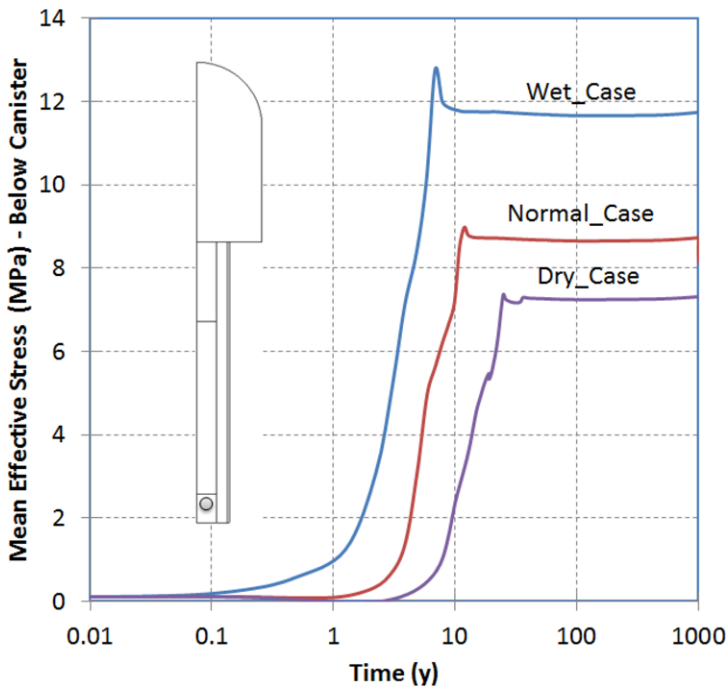


Fig. 10 Evolution of the mean effective stress in three cases (location: under the canister). Time from canister emplacement.

COUPLED THM MODELLING

as the section where stress is plotted is close to the fracture. In the case of high intrinsic permeability of rock, water flows from the rock to the buffer in a much faster way. The time to reach a stabilized stress and the values achieved are different between the three cases. A lower intrinsic permeability of rock delays the process of swelling and, hence, the effective stress development. A larger effective stress is developed below the canister as saturation takes place faster. This can be explained by the fact that backfill is more rigid during buffer swelling in the Wet_Case compared to the Normal_Case. The same behaviour is observed if the Normal_Case is compared with the Dry_Case.

Figure 11 shows the swelling pressure of the backfill (central zone) for the three cases. As this zone is far away from the fracture, the time to achieve the maximum swelling pressure of the central backfill mainly depends on the intrinsic permeability of the rock and not on the water entry from the fracture. In the Wet_Case, the swelling pressure of the central backfill reaches a value of 7.5 MPa and stabilizes at 6 MPa. Except for the Dry_Case, the other two cases reach a peak value of mean effective stress at the same time. The reason for this is that the intrinsic permeability of the rock is

of greater importance with respect to the time required to reach full saturation of the backfill. However, the swelling of the buffer blocks and the ring is greater in the Wet_Case. As a result, the achieved stress in the backfill is greater in the Wet_Case, despite it taking the same time to reach full saturation as the Normal_Case.

The peak that appears in the evolution of effective stress is caused by the effect of unloading after saturation. Once saturation is reached, the maximum effective pressure is achieved. Then, pore pressure becomes higher than atmospheric pressure and, as the material is saturated, effective stresses come into play. The increase in pore pressure implies a decrease in effective stresses. This is represented in Figure 12, which shows the suction–mean effective stress path. Although suction is a positive definite variable, the negative values have been represented in order to highlight the fact that effective stress decreases after full saturation of the medium.

Figure 13 shows the evolution of vertical displacements at the buffer–backfill interface for the three cases. The vertical displacements are generated by the swelling of the buffer blocks. Displacements are mainly concentrated at the

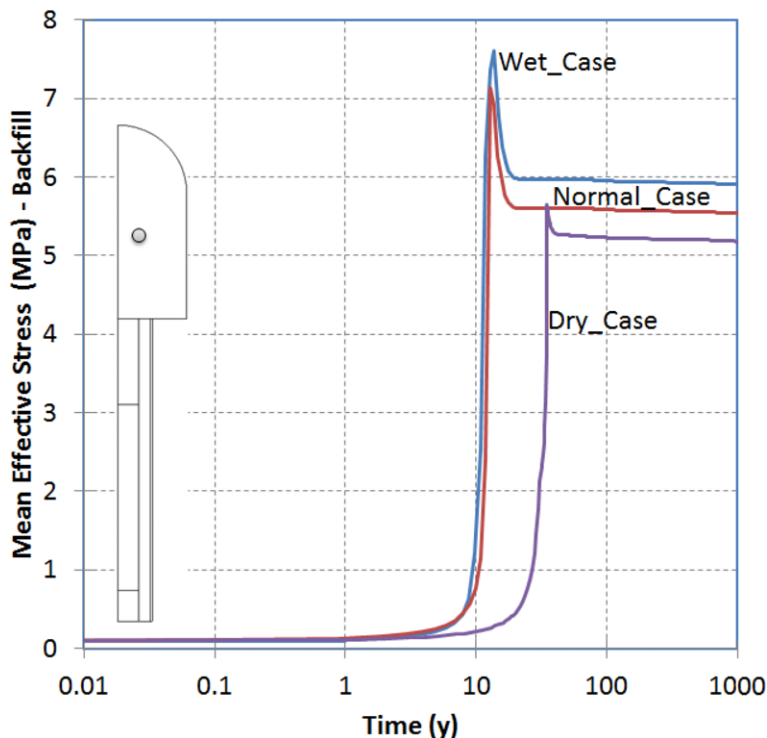


Fig. 11 Evolution of the mean effective stress in three cases (location: central backfill). Time from canister emplacement.

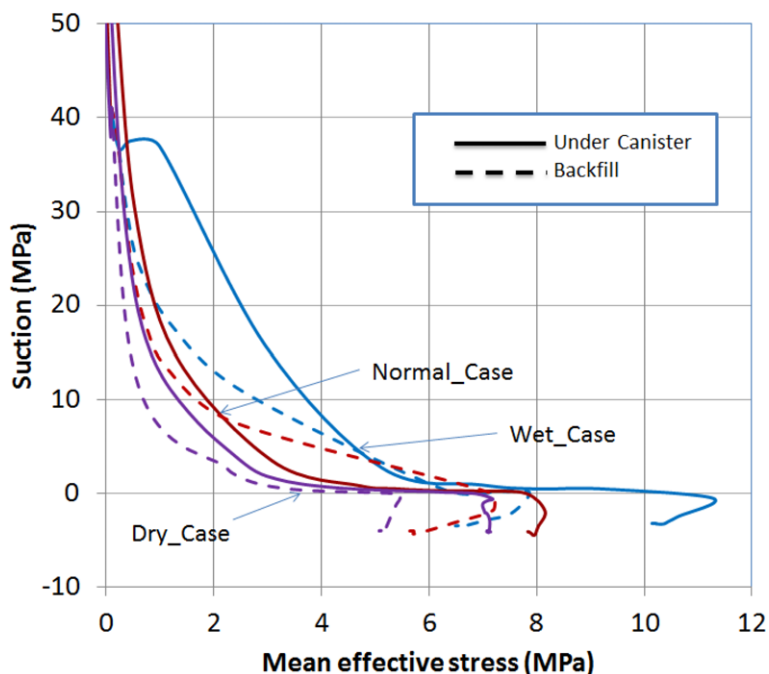


Fig. 12 Suction v. mean effective stress path for a point below the canister and a point in the backfill. Negative suctions are included to show that after saturation the mean effective stress decreases due to the development positive pore pressure.

buffer–backfill interface. Owing to the swelling, the buffer blocks push the backfill up. In the case of the dry deposition hole (Dry_Case), as the swelling of buffer blocks takes place slowly, the achieved displacements at the interface show a lower value. In other words, the buffer and backfill swell in a more simultaneous way for the Dry_Case compared to the Normal_Case and Wet_Case for which the buffer hydrates more rapidly than the backfill.

As a conclusion, it can be said that owing to the delay in water supply in the Dry_Case, displacements take place later compared to the other two cases. The maximum buffer–backfill interface displacement peak is about 5–6 cm in the Dry_Case. In the Wet_Case, vertical displacements reach to 9–10 cm, and for the Normal_Case they are the range of 7–8 cm.

Table 7 summarizes the results in terms of the maximum temperatures achieved, times to reach saturation, saturated density of the buffer and backfill, stress development, and maximum displacements. The Dry_Case curve for temperature shows an early peak (absolute maximum) that is caused by the lower thermal conductivity of the open gap, which remains open for a longer time compared to the other cases. Earlier saturation is motivated by the presence of the highly conductive zone that

simulates a fracture. Final densities show little variation. As the global volumetric deformation of the engineered barrier is nearly zero (except for the deformation of the rock, which is very small), mean effective stress development is of the same order of magnitude as the swelling pressure. There are differences, however, as the saturation of the engineered barrier takes place in different ways depending on the conditions of hydration (intrinsic permeability and fractures, and the shape of the buffer–backfill system). A greater development of stresses is calculated with the Wet_Case. Finally, displacement at the interface is influenced by the earlier or later expansion of the buffer.

Results for 3D modelling

In this section, some results for 3D modelling are presented in order to check the influence of the simplification performed in the axisymmetrical models. For simplicity, the 3D geometry does not take into account the presence of either the pellets or the air-gap element. Besides this, backfill tunnel has a greater volume compared to the 2D calculations. The BBM parameters used for the buffer and backfill are the same as in the previous 2D

COUPLED THM MODELLING

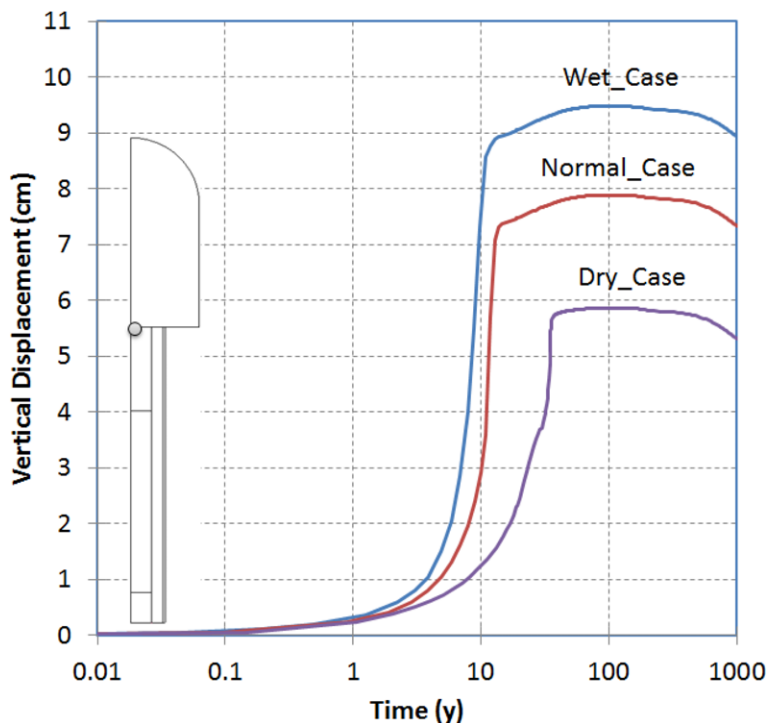


Fig. 13. Evolution of vertical displacement in three cases (location: the buffer–backfill interface). Time from canister emplacement.

axisymmetrical calculations. The value of the intrinsic permeability for the rock corresponds roughly to the Dry_Case ($1.52 \times 10^{-20} \text{ m}^2$), the intrinsic permeability of the backfill is the same as in the previous cases, and the intrinsic permeability of the buffer is higher but is in the range of typical values for bentonite. So, the values chosen fall in the same order of magnitude of intrinsic permeability and this is favourable for the numerical solution, especially for the 3D model with a relatively simple mesh. Further work on mesh optimization is required in order

to obtain 3D solutions of the THM problem, with barriers having greater contrasts in permeability.

Figure 14 shows a comparison between the 2D and the 3D case in terms of the total mean stress. As the backfill tunnel has a greater volume for the 3D geometry, the whole system needs more time to reach full saturation. Therefore, the generated stresses reach the steady-state conditions in faster times in the case of 2D calculations. The values achieved for the total mean stresses are in the same range (i.e. from 8 to 12 MPa).

Table 7. Comparison of three cases (2D axisymmetrical cases)

Analysed parameters	Units	Wet_Case	Normal_Case	Dry_Case
Temperature maximum at the bentonite ring	°C	82.5	82.5	82.5
Temperature maximum at the canister	°C	82.5	82.5	84.0
Time to reach full saturation of the bentonite discs – under the backfill	Years	10.0	12.7	32.5
Time to reach full saturation of the backfill – central zone	Years	10.0	12.7	34.0
Saturated density of the backfill (average)	kg m^{-3}	2156	2156	2156
Saturated density of the buffer (average)	kg m^{-3}	1999	1991	1994
Swelling pressure of the bentonite discs under the canister	MPa	11.7	8.7	7.2
Swelling pressure of the backfill – central	MPa	6.2	5.5	5.0
Displacements at the buffer–backfill interface	cm	9.0	7.4	5.3

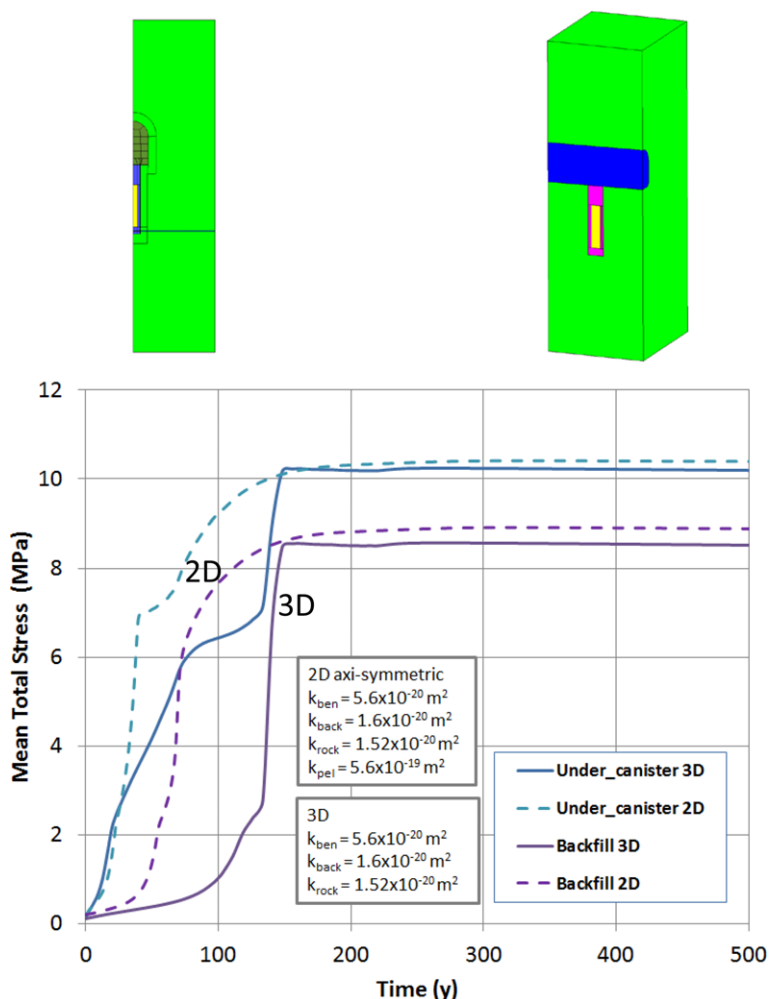


Fig. 14 Evolution of the mean total stresses in 2D and 3D modelling. Time from canister emplacement.

Conclusions

The laboratory tests (oedometer and infiltration) performed by B + Tech Oy (Finland) were modelled using the finite-element code Code_Bright. The Barcelona Basic Model (BBM) was used to model the mechanical constitutive behaviour of the MX-80 bentonite and Friedland clay, together with Darcy's law for the flow. The parameters obtained from the modelling of laboratory tests were used to perform 2D and 3D sensitivity analyses for the final disposal of nuclear spent fuel.

The values in the Table 7 correspond to representative points for the axisymmetrical cases. In the Dry_Case, the gap between the canister and the buffer closes later compared to the other cases. The maximum temperature in the canister

reaches a value of 84°C for the Dry_Case (compared to 82.5°C), which is a clear effect of the air-gap element. As discussed throughout this paper, the fractures and hydraulic conductivity of rock have an impact on the results obtained in terms of maximum temperatures, swelling stress and displacements.

The buffer-backfill interface has been analysed and the maximum vertical displacement has the same order of magnitude as the one calculated previously by Leoni (2013).

With respect to the 3D calculations, the system reaches steady-state conditions later than in the 2D axisymmetrical models, mainly because the backfill volume is larger. However, the values obtained for stresses in the 3D models are in the same range as in the 2D calculations.

COUPLED THM MODELLING

The present research work was financed in part by B + Tech Oy (Finland) under a POSIVA Oy project. The authors especially thank Jorma Autio from B + Tech and Kari Koskinen from Posiva for their support with the administrative tasks necessary to carry out this project, and for their comments and suggestions during this work.

References

- ÅKESSON, M., KRISTENSSON, O. & BÖRGESSON, L. 2010. *SR-Site Data Report. THM Modelling of Buffer, Backfill and Other System Components. Critical Processes and Scenarios*. SKB TR-10-11. Svensk Kärnbränslehantering AB (SKB), Stockholm, Sweden, <http://www.skb.com/publication/2095121/TR-10-11.pdf>
- ALONSO, E.E., GENS, A. & JOSA, A. 1990. A constitutive model for partially saturated soils. *Géotechnique*, **40**, 405–430.
- BÖRGESSON, L., FREDRIKSON, A. & JOHANNESON, L.-E. 1994. *Heat Conductivity of Buffer Materials*. SKB TR 94-29. Svensk Kärnbränslehantering AB (SKB), Stockholm, Sweden, <http://www.skb.com/publication/11249/TR94-29.pdf>
- HAGROS, A., AIKAS, K., MCEVVEN, T. & ANTTILA, P. 2003. *Host Rock Classification*. Working Report 2003-04. Posiva, Eurajoki, Finland, http://www.posiva.fi/files/2183/POSIVA-2003-04_Working-report_web.pdf
- HÖKMARK, H., LÖNNQVIST, M., KRISTENSSON, O., SUNDBERG, J. & HELLSTRÖM, G. 2009. *Strategy for Thermal Dimensioning of the Final Repository for Spent Nuclear Fuel*. SKB Report R-09-04. Svensk Kärnbränslehantering AB (SKB), Stockholm, Sweden.
- IKONEN, K. 2003. *Thermal Analyses of Spent Nuclear Fuel Repository*. Posiva Report 2003-04. Posiva, Eurajoki, Finland.
- JUVANKOSKI, M., IKONEN, K. & JALONEN, T. 2012. *Buffer Production Line 2012. Design, Production and Initial State of the Buffer*. Posiva Report 2012-17. Posiva, Eurajoki, Finland.
- KETO, P., HASSAN, M. ET AL. 2013. Backfill production line 2012. In: KETO, P. (ed.) *Design, Production and Initial State of the Deposition Tunnel Backfill and Plug*. Posiva Report 2012-18. Posiva, Eurajoki, Finland.
- KIVIRANTA, L. & KUMPULAINEN, S. 2011. *Quality Control and Characterization of Bentonite Materials*. Posiva Working Report 2011-84. Posiva, Eurajoki, Finland, http://www.posiva.fi/files/1994/WR_2011-84_web.pdf
- KIVIRANTA, L., KUMPULAINEN, S., PINTADO, X., KARTTUNEN, P. & SCHATZ, T. 2016. *B + Tech Oy, Characterization of Bentonite and Clay Materials 2012–2015*. Posiva Working Report WR 2016-05. Posiva, Eurajoki, Finland.
- LEONI, M. 2013. *2D and 3D Finite Element Analysis of Buffer–Backfill Interaction*. Posiva Report 2012-25. Posiva, Eurajoki, Finland.
- MARJAVAARA, P. & KIVIKOSKI, H. 2011. *Filling the Gap Between Buffer and Rock in the Deposition Hole*. Posiva Working Report 2011-33. Posiva, Eurajoki, Finland, http://www.posiva.fi/files/1923/WR_2011-33web.pdf
- OLIVELLA, S., CARRERA, J., GENS, A. & ALONSO, E.E. 1994. Nonisothermal multiphase flow of brine and gas through saline media. *Transport in Porous Media*, **15**, 271–293.
- OLIVELLA, S., GENS, A., CARRERA, J. & ALONSO, E.E. 1996. Numerical formulation for a simulator (CODE BRIGHT) for the coupled analysis of saline media. *Engineering Computations*, **13**, 87–112.
- PINTADO, X. & RAUTIOAHO, E. 2013. *Thermo-Hydraulic Modelling of Buffer and Backfill*. Posiva Report 2012-48. Posiva, Eurajoki, Finland.
- PINTADO, X., MAMUNUL, H.M.D. & MARTIKAINEN, J. 2013. *Thermo-Hydro-Mechanical Tests of Buffer Material*. Posiva Report 2012-49. Posiva, Eurajoki, Finland.
- POSIVA 2013. *Safety Case for the Disposal of Nuclear Spent Nuclear Fuel at Olkiluoto*. Posiva Report 2013-01. Posiva, Eurajoki, Finland.
- RAIKO, H. 2012. *Canister Design*. Posiva Report 2012–13. Posiva, Eurajoki, Finland, http://www.posiva.fi/files/3093/POSIVA_2012-13.pdf
- TANG, A.-M., CUI, Y.-J. & LE, T.-T. 2007. A study on the thermal conductivity of compacted bentonites. *Applied Clay Science*, **41**, 181–189.
- TOPRAK, E., MOKNI, N., OLIVELLA, S. & PINTADO, X. 2013. *Thermo-Hydro-Mechanical Modelling of Buffer, Synthesis Report*. Posiva Report 2012-47. Posiva, Eurajoki, Finland.
- VAN GENUCHTEN, M.Th. 1980. A closed equation for predicting the hydraulic conductivity of unsaturated soils. *Soil Science Society of America Journal*, **44**, 892–898.